Intermetallic Nanocatalysts from Heterobimetallic 10–14 Pyridine-2-Thiolate Precursors

Carena L. Daniels,[1] Megan Knobeloch,[1] Philip Yox,[1] Marquix A. S. Adamson,[1] Yunhua Chen,[1] Rick W. Dorn,[1,2] Hao Wu,[3,4] Guoquan Zhou,[3,4] Huajun Fan,[3,4] Aaron J. Rossini,[1,2] and Javier Vela*[,1,2]

[1]Department of Chemistry, Iowa State University, Ames, Iowa 50011, United States. [2]Ames Laboratory, Ames, Iowa 50011, United States. [3]School of Materials and Chemical Engineering, Ningbo University of Technology, Ningbo, Zhejiang, P. R. China. [4]College of Chemical Engineering, Sichuan University of Science and Engineering, Zigong, Sichuan, P. R. China.

KEYWORDS. Heterobimetallic, single-source precursors, 10–14 intermetallics, azoxyarenes, catalysis.

ABSTRACT: Intermetallic compounds are atomically ordered inorganic materials containing two or more transition metals and main group elements in unique crystal structures. Intermetallics based on group 10 and group 14 metals have shown enhanced activity, selectivity, and durability compared to simple metals in many catalytic reactions. While high temperature solid-state methods to prepare intermetallic compounds exist, softer synthetic methods can provide key advantages, such as enabling the preparation of metastable phases, or of smaller particles with increased surface areas for catalysis. Here, we study a generalized family of heterobimetallic precursors to binary intermetallics, each containing a group 10 and metal a group 14 tetrel bonded together and supported by pincer-like pyridine-2-thiolate ligands. Upon thermal decomposition, these heterobimetallic complexes form 10-14 binary intermetallic nanocrystals. Experiments and density functional theory (DFT) computations help in better understanding the reactivity of these precursors toward the synthesis of specific intermetallic binary phases. Using Pd_2Sn as an example, we demonstrate that nanoparticles made in this way can act as uniquely selective catalysts for the reduction of nitroarenes to azoxyarenes, which highlights the utility of the intermetallics made by our method. Employing heterobimetallic pincer complexes as precursors toward binary nanocrystals and other metal-rich intermetallics provides opportunities to explore the fundamental chemistry and applications of these materials.

INTRODUCTION

Intermetallic compounds are composition specific materials where two or more metals crystallize in ordered structures that are distinct from those adopted by the constituent elements. Along with adopting unique structures, intermetallic compounds are known to possess many interesting properties including magnetism, superconductivity, shape memory, hydrogen sorption, and catalytic activity.[1,2,3,4] For example, compared to simple, single element metals, binary 10–14 intermetallics show enhanced catalytic activity, selectivity, and durability.[5,6,7] Among these, Pt-Sn nanocatalysts such as Pt_3Sn and PtSn have been studied for a variety of reactions including alkane dehydrogenation,[8,9,10,11,12,13,14,15,16,17,18,19,20] electro-oxidation of CO, formic acid, and methanol fuel cells,[21,22,23,24,25,26] methane conversion to ethylene, benzene, and napththalene,[27] dehydroisomerization of butane to isobutene,[28] and highly selective hydrogenation of nitrobenzene to aniline,[29] 3-nitrostyrene to 3-aminostyrene,[30] and of furfural to furfuryl alcohol.[31] Less studied are Pd-Sn and Ni-Sn binaries. Nonetheless, PdSn is known to catalyze the electrooxidation of formic acid for fuel cells,[32,33] and Pd_2Sn the ethanol oxidation reaction (EOR) in direct alcohol fuel cells,[34] as well as the denitration of water.[35] In addition, Ni_3Sn, Ni_3Sn_2 and Ni_3Sn_4 catalyze acetylene hydrogenation,[36] and Ni_3Sn the decomposition of methanol for the production of hydrogen.[37]

Other binary and multinary 10–14 intermetallics promise to be just as interesting. Germanides $Ni_{19}Ge_{12}$, Pt_3Ge, and $PtGe_2$ catalyze the hydrogen evolution reaction (HER) under acidic conditions.[38,39] Pd_2Ge nanoparticles are active in ethanol oxidation for fuel cell applications,[40] where they are stable for up to 250 cycles. Nickel silicides have also received attention, for example $Ni_{31}Si_{12}$, Ni_2Si, $NiSi_2$, and NiSi in hydrogenation reactions.[41,42,43,44,45] Ni_2Si and Pd_2Si were investigated for HER,[46] and for selective phenylacetylene hydrogenation.[47] Recently, ternary silicide intermetallics such as LaScSi, LaCoSi, and LnNiSi (Ln = La-Nb) have gathered attention due to their ability to act as electrides—compounds which have anionic-like electrons localized in interstitial sites—which renders them useful in hydrogen storage as well as in catalytic ammonia synthesis at moderate temperature (400 °C) and pressure (1 atm).[48,49,50,51,52]

While many high temperature solid state methods to synthesize intermetallic compounds exist, low-temperature solution-phase methods provide some advantages, for example in enabling the preparation of metastable phases, or of intermetallics with smaller particle sizes with increased

surface areas for catalytic applications.[2,3,4] Foremost among such "soft" chemistry routes is polyol co-reduction, where soluble metal precursors are heated in ethylene glycol or another mildly reducing solvent, usually to produce the desired intermetallic compound.[53,54,55,56,57,58,59,60] While the use of this method is widespread, it may result in phase segregated products due to the different reduction potentials of the metals. Another synthetic method, which is a modification of the polyol approach is coined 'ship-in-a-bottle'.[31] In this method, a mesoporous silica shell is grown around a metal nanoparticle, followed by the addition of a second metal precursor to form the intermetallic product inside the mesoporous shell. The intermetallic nanoparticles made in this way are more stable against aggregation and can stand higher temperatures during catalysis. However, this is a longer, multistep process, and the resulting products may also suffer from partial phase segregation.

Recently, we prepared binary 10–15 and 11–15 intermetallics through the use of heterobimetallic precursors.[61] Rather than starting with two separate metallic precursors and reducing them together, this approach uses premade complexes where two metals are already present and bonded together.[62,63,64,65,66,67,68] In this work, we study the solid-state decomposition of a family of group 10-14 heterobimetallic complexes as precursors to the preparation of 10-14 intermetallic compounds. Our approach is related to the use of single-source precursors (SSPs), which are commonly employed in chemical vapor deposition in order to lower decomposition temperatures and prevent phase segregation.[69,70] However, our approach differs from SSPs in that the stoichiometry of the final inorganic phase that is produced may or may not be the same as the initial ratio of the two metals in the heterobimetallic precursor, as dictated by the reactivity of the specific complex and reaction conditions used (see below). Here, we use experiments and density functional theory (DFT) to better understand the effect of the heteronucleating pyridine-2-thiolate and ancillary phosphorous-based ligands on the formation of different binary intermetallic phases. Finally, we test Pd_2Sn nanoparticles made in this way as catalysts for the selective hydrogenation of nitroarenes, which demonstrates the utility of the intermetallics synthesized by our method.

RESULTS AND DISCUSSION

Precursor Design and Screening. A family of pyridine-2-thiolate-based heterobimetallic complexes containing tetrel elements Ge and Sn bonded to transition metals Ni, Pd, and Pt, pictured in Figure 1a was synthesized and thermally decomposed to form intermetallic nanoparticles. In order to find suitable heterobimetallic complexes to screen as possible single-source precursors to 10–14 intermetallics, we searched the Cambridge Structural Database (CSD).[71] First, we looked for crystallographically characterized complexes that contained both group 10 and group 14 metals, ideally already bonded to each other. We did not place any restrictions on the metal-metal bond distance nor the order of the bond. Next, we grouped the initial results into families of complexes supported by similar ligands. We then narrowed our search to include only complexes with easily substituted—and thus potentially tunable—elements and ligands. Our search yielded four distinct families of complexes shown in Figure 1.[72,73,74,75] Because of the wide variety of elemental and ligand substitutions that it afforded, as well as because of its general ease of synthesis, we decided to focus our efforts on bis(pyridine-2-thiolate)-based family of heterobimetallic complexes shown in Figure 1a.

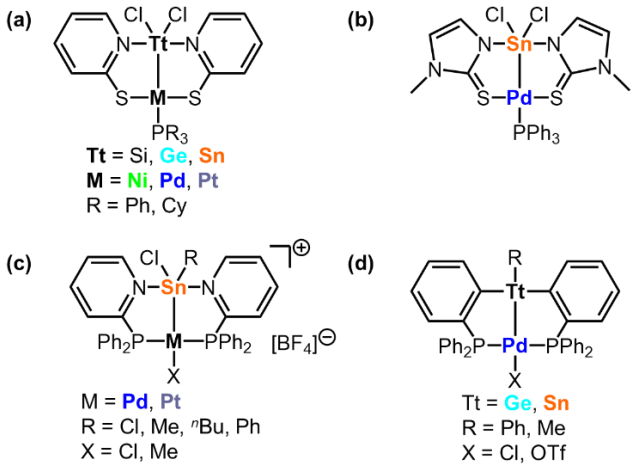

Figure 1. Families of group 10–14 heterobimetallic complexes found in the CSD.

In this family of complexes, a group 10 transition metal (Ni, Pd, Pt) and a group 14 (tetrel = Ge, Sn) are held together by two-bridging pyridine-2-thiolate ligands. The heterobimetallic unit is further capped by two halides (normally chlorides or pseudohalides, see below) on the tetrel side, and a phosphorous-based ligand (alkyl or aryl phosphine or phosphite) on the transition metal side (Chart 1). Previous studies examined the appropriate resonance assignment for the pyridine-2-thiolate ligands in these complexes (see below).[72] Based on crystallographic and computational (density functional theory) data, it was determined that the tetrel (Tt) in these complexes normally acts as an X-type ligand, but can become more Z- or L-type depending on ligand substitution (see further discussion below).[72]

Synthesis of Heterobimetallic Precursors. The 10–14 heterobimetallic complexes have been made by reacting $Cl_2Tt(pyridine\text{-}2\text{-}thiolate)_2$ (Tt = Ge, Sn) and $M(PPh_3)_4$ (M = Pd, Pt) (for M = Ni, $Ni(cod)_2$ and an excess of PPh_3 are first mixed *in situ*) (Scheme 1a).[72] We find this route is reproducible, and often resorted to it in order to prepare *ca.* half of—the previously reported—complexes in Chart 1. Another route used to make M-Sn complexes (M = Pd, Pt) involves reacting $Sn(Py)_2$ with $MCl_2(PPh_3)_2$ (not shown).[72] For the sake of synthetic ease, we have developed a slightly simpler, more flexible route that consists of reacting together stoichiometric amounts of $Cl_2Tt(pyridine\text{-}2\text{-}thiolate)_2$ (Tt = Ge, Sn), a soluble zerovalent metal precursor $M(L)_2$ (M = Pd, Pt), and one equivalent of PR_3 (phosphine, R = Ph, Cy, *n*Bu; phosphite R = OPh) (Scheme 1b). By avoiding the use of excess phosphine, we find that this route enables an easier preparation and purification of a wider range of heterobimetallic complexes.

Scheme 1. Synthetic routes to bis(pyridine-2-thiolate) heterobimetallic complexes.

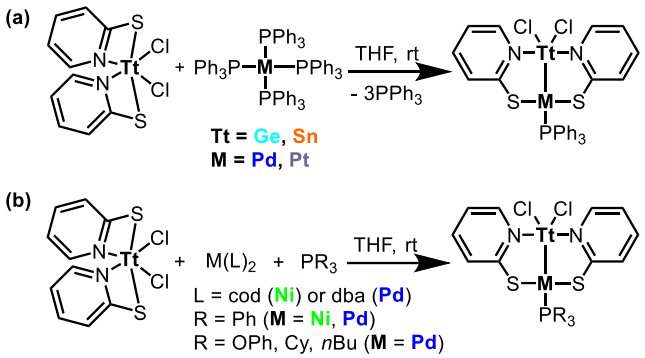

Using this approach, we were able to expand the range of pyridine-2-thiolate heterobimetallic complexes to Ge-Ni and Ge-Pt analogs for the first time (Table 1 and Table S1). The molecular structures of two of these new complexes, (**1**) and (**3**), respectively were obtained by single crystal X-ray diffraction and are shown in Chart 1. In addition, we used this approach in altering the nature of the M-capping phosphine ligand. In the case of the Sn-Pd complexes, PPh_3 was previously exchanged in solution by exposure to an excess of the better σ-donor PCy_3.[72] Here, we were able to use the new approach outlined above, in Scheme 1b, to explore a wider range of heterobimetallic Sn-Pd complexes capped with PCy_3, $P(OPh)_3$, and P*n*Bu_3. Interestingly, during the isolation of the P*n*Bu_3 complex, a byproduct where one of the tin-bound chlorides (Cl^-) was replaced by a pyridine-2-thiolate group—formally, a pseudohalide—crystallized preferentially. The molecular structures of the $P(OPh)_3$ complex (**8**), and of the "scrambled" P*n*Bu_3 complex (**9**) obtained by single crystal X-ray diffraction analysis are shown in Chart 1 (also Table 1 and Table S1).

The heterobimetallic complexes (**1**), (**3**), and (**8**) display a pseudo-trigonal bipyramidal geometry around the tetrel (Tt), with the pyridine nitrogens (N's) in pseudoaxial positions (the N-Tt-N angles are between 163–170°, see Table 1). In turn, the two chlorides and the group 10 metal (M) occupy pseudoequatorial positions around Tt (the X-Tt-X and X-Tt-M angles are between 100–110° and *ca.* 126°, respectively). Interestingly, the scrambled compound (**9**) containing the tripodal tris(pyridine-2-thiolate) $Tt(PyS)_3$ ligand is a special case. Specifically, the N on the "free" PyS arm points toward the heterobimetallic Sn-Pd core. Curious about whether this was due to any N-Sn or N-Pd interactions, we measured both of these distances and compared them each to the corresponding sum of their van der Waals radii (Table 1). Both of these distances were under this sum (2.6463(58) Å *vs.* 3.85 Å, for N-Sn and 3.5643(54) Å *vs.* 3.65 Å for N-Pd),[76] suggesting there is, indeed, N-Sn and N-Pd bonding interactions in the solid state (thus increasing the apparent coordination number around Sn to 6 and Pd to 5 in this complex). Interestingly, (**9**) shows only one set of PyS resonances by ^1H and ^{13}C NMR in dmso-d_6, suggesting fast exchange of the bound and "free" PyS arms in solution. To best describe the geometry around the group 10 transition metals (M) in these complexes, we used a tau parameter, τ = (Σangles around M - 360°) / (438° - 360°).[77,78] In this way, a perfect square planar geometry has a τ = 0, whereas a perfect tetrahedral geometry has a τ = 1. In all the heterobimetallic complexes, the sum of the angles of M is approximately 360°, and thus tau is very close to τ ≃ 0 (fairly square planar).

Insights from Computations. In order to gain a better understanding of the Ge-M and Sn-M heterobimetallic complexes (M = Ni, Pd, Pt), as well as their hypothetical Si-M analogs and a few Sn-Pd complexes with different phosphorous ligands, we studied them computationally using density functional theory (DFT). For all complexes, the popular B3LYP with hybrid exchange functional[79] was used to optimize their molecular geometries, while an additional functional, TPSS,[80] was used on $Cl_2Sn(\mu\text{-PyS})PdPPh_3$ (**5**) (see Experimental). The optimized geometries show a relatively flat Tt-(μ-pyS)$_2$-M frame, with the phosphorous center adopting a pseudo-tetrahedral geometry.

A careful look at some of the key computationally optimized Tt-M, Tt-N, M-S, M-P (Tt = Si, Ge, Sn; M = Ni, Pd, Pt) bond distances show they overestimate those determined experimentally from the crystal structures by *ca.* 2.6%, however, both follow similar trends (Figure 2 and Table 2). Generally, Tt-N bond distances stay relatively the same for compounds with the same group 14 element (Tt). Tt-M, M-S, and M-P bond distances increase as the group 10 metal (M) get larger. When keeping M constant, increasing the size of the Tt leads to longer Tt-M and Tt-N bond distances, while M-S and M-P distances stay the same.

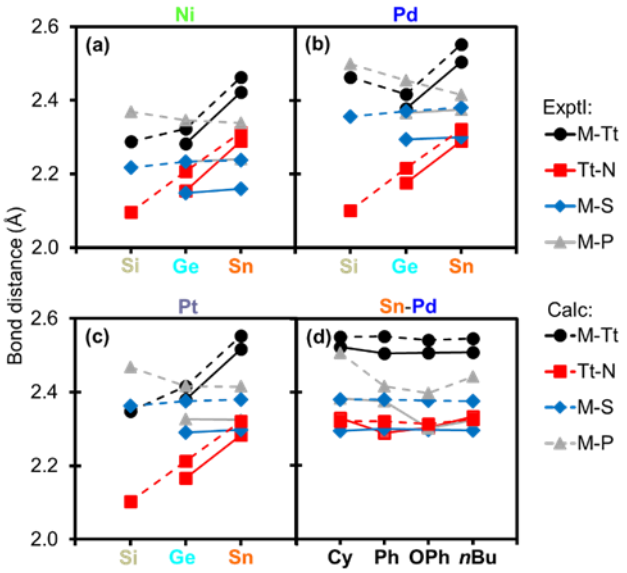

Figure 2. Selected bond distances for (a) $Cl_2Tt(\mu\text{-PyS})NiPPh_3$, (b) $Cl_2Tt(\mu\text{-PyS})PdPPh_3$, (c) $Cl_2Tt(\mu\text{-PyS})PtPPh_3$ with Tt = Si, Ge, and Sn, and (d) $Cl_2Sn(\mu\text{-PyS})PdPR_3$ with R = Cy, Ph, OPh, and *n*Bu_3.

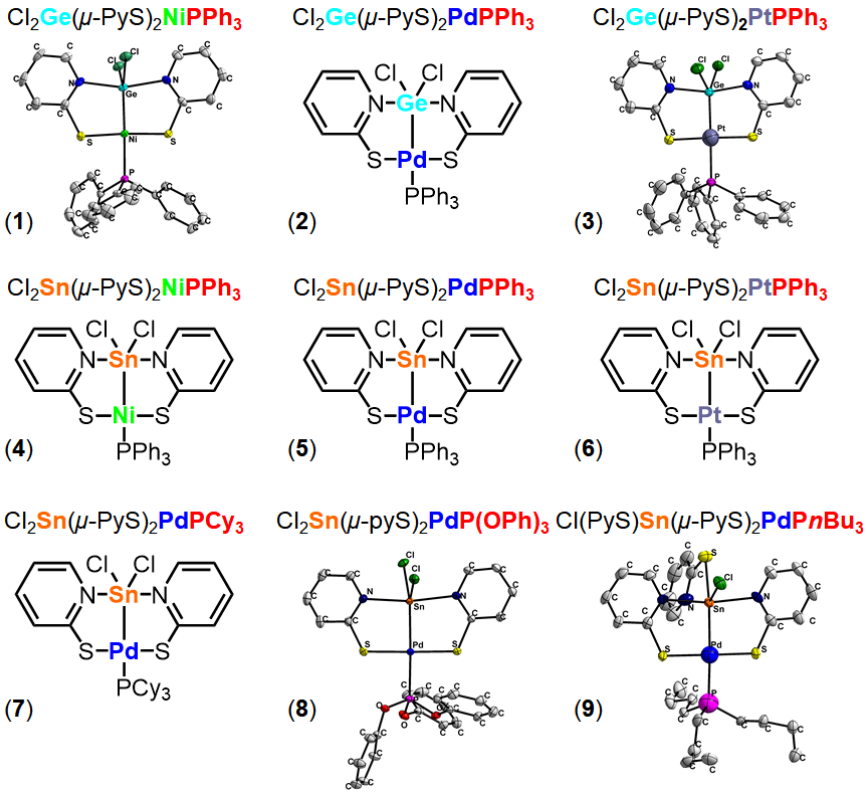

Chart 1. Family of pyridine-2-thiolate-based heterobimetallic complexes studied as precursors in this work. Oak Ridge Thermal Ellipsoid Plot (ORTEP) diagrams at 50% probability are shown for compounds (**1**), (**3**), (**8**), and (**9**), which were crystallographically characterized here (see Experimental). Compounds (**2**),[72] and (**4**-**7**),[72,81] were reported previously.

Table 1. Selected bond lengths and angles for new 10–14 heterobimetallic complexes.

Parameter (Å or °)[a]	$Cl_2Ge(\mu\text{-}PyS)_2NiPPh_3$ (**1**)	$Cl_2Ge(\mu\text{-}PyS)_2PtPPh_3$ (**3**)	$Cl_2Sn(\mu\text{-}PyS)_2PdP(OPh)_3$ (**8**)	$Cl(PyS)Sn(\mu\text{-}PyS)_2PdPnBu_3$ (**9**)
M-Tt	2.2766(16)	2.379(3)	2.5067(3)	2.5087(5)
M-S_1	2.148(2)	2.2990(7)	2.2939(7)	2.3016(13)
M-S_2	2.143(2)	2.2809(8)	2.3001(7)	2.2885(13)
M-P	2.2245(18)	2.3262(6)	2.3017(7)	2.3243(14)
Tt-N_1	2.157(4)	2.195(2)	2.296(2)	2.362(4)
Tt-N_2	2.161(4)	2.137(2)	2.311(2)	2.304(4)
Tt-Cl_1	2.2084(19)	2.2157(6)	2.3823(7)	2.4237(13)
Tt-X (X = Cl_2 or S)[b]	2.2283(19)	2.2001(7)	2.3608(6)	2.4744(16)
Pd---N_3	n.a.	n.a.	n.a.	3.5643(54)[c]
Sn---N_3	n.a.	n.a.	n.a.	2.6463(58)[c]
P-M-Tt	178.41(5)	174.895(16)	176.121(19)	177.83(4)
P-M-S_1	89.63(6)	89.26(2)	92.10(2)	91.18(5)
P-M-S_2	87.04(6)	89.10(2)	89.07(2)	88.62(5)
S_1-M-S_2	173.79(6)	177.26(2)	177.67(3)	174.38(5)
S_1-M-Tt	91.41(6)	90.20(2)	89.337(17)	90.94(4)
S_2-M-Tt	91.89(6)	91.633(19)	89.368(19)	89.23(4)
M-Tt-N_1	98.62(10)	96.40(6)	95.17(5)	94.11(11)
M-Tt-N_2	98.257(11)	98.43(6)	94.90(6)	96.05(10)
N_1-Tt-N_2	163.12(13)	165.14(9)	169.60(8)	169.61(15)
Cl_1-Tt-X[b]	109.80(6)	108.25(3)	100.56(2)	95.08(6)
Cl_1-Tt-M	125.98(6)	126.28(2)	125.573(18)	118.85(4)

X-Tt-M	124.22(6)	125.39(2)	133.815(19)	145.78(4)

[a]M = Ni, Pd, or Pt (group 10); Tt = Ge or Sn (group 14). [b]X = Cl or S. [c]ΣvanderWaalsradii: Pd+N = 3.65 Å, Sn+N = 3.85 Å.[76]

In the case of the Sn-Pd complexes, the C-S bond distance increases from R = OPh < Cy ~ Ph < *n*Bu. We also calculated the Wiberg bond orders for these complexes to measure the electron density between the atoms.[82] The Wiberg bond order at S reveals this is accompanied by a shifting of the electron density. The bond order around S increases from R = Cy ~ *n*Bu < Ph < OPh. Natural Bond Orbital (NBO) analysis suggests the electron density increases at S center from R = OPh < Ph < *n*Bu < Cy.

Importantly, using computations we were able to assess the relative strength of different interactions within a series of 10–14 heterobimetallic complexes. Interestingly, the cost of breaking one of Tt-N (pyridine) bonds is relatively small, ranging from 1.38 kcal/mol for the $Cl_2Si(\mu$-$PyS)NiPPh_3$ complex, to 8.99 kcal/mol for the $Cl_2Ge(\mu$-$pyS)_2PtPPh_3$ complex, and becoming prohibitively high for the $Cl_2Sn(\mu$-$pyS)_2PtPPh_3$ complex. We were also able to estimate overall metal (M) binding energies according to the general Scheme 2. In this way, the metal binding energies calculated for $Cl_2Sn(\mu$-$pyS)_2Pd(PR_3)$ increase in the order: $PnBu_3 < PCy_3 < P(NMe_2)_3 < P(OPh)_3 < P(C_6F_5)_3 < PPh_3$ (Table 2).

Scheme 2. Calculation of overall metal binding energies from the dissociation of $Cl_2Sn(\mu$-$pyS)_2Pd(PR_3)$ into $Cl_2Sn(\mu$-$PyS)_2$ (L), Pd, and PR_3 (R = Cy, Ph, OPh, or nBu$_3$).

$$LPdPR_3 \longrightarrow L + Pd + PR_3$$

Thermolysis of Heterobimetallic Precursors. To assess their potential as precursors to intermetallic compounds, we studied the solid-state thermal decomposition of all the Ge- and Sn-based heterobimetallic complexes shown in Chart 1. Differential scanning calorimetry (DSC) and thermogravimetric analysis (TGA) were simultaneously monitored from near 21 °C (room temperature or R.T.) to 600 °C—in all cases, under an inert dry-nitrogen (N_2) atmosphere (Figure 3 and Table 3). After cooling to R.T., the leftover solid residue was further analyzed by powder X-ray diffraction (XRD). In general, these heterobimetallic compounds undergo thermally-induced decomposition between 240 and 325 °C, before mass loss eases and a plateau is reached around 400–500 °C (Figure 3).

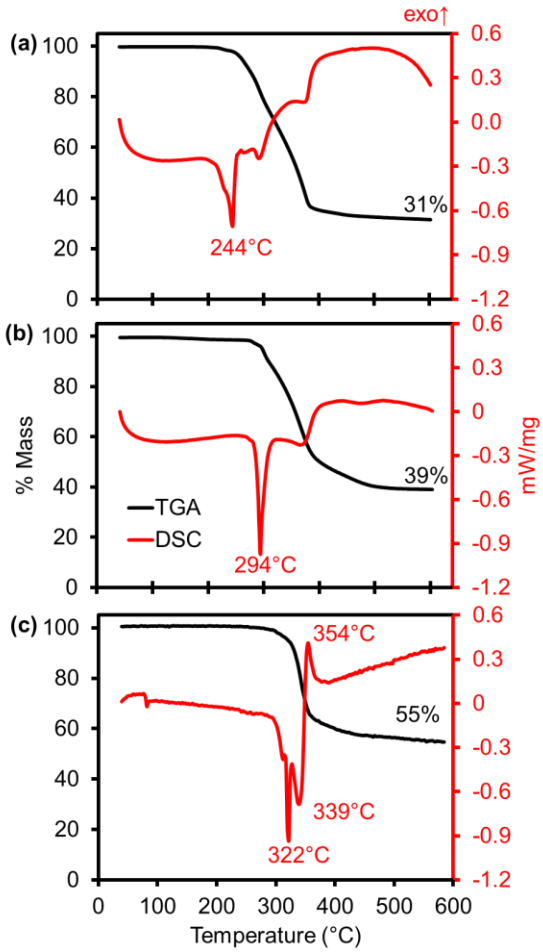

Figure 3. TGA and DSC for (a) $Cl_2Ge(\mu$-$PyS)_2PdPPh_3$ (**2**), (b) $Cl_2Sn(\mu$-$PyS)_2PdPPh_3$ (**5**), and (c) $Cl_2Sn(\mu$-$PyS)_2PtPPh_3$ (**6**) upon heating from 40–600 °C.

XRD analysis of the solid products left behind after decomposition shows that both Ni complexes, specifically Ge-Ni (**1**) and Sn-Ni (**4**) complexes produced oxides and sulfides, respectively, rather than one of the originally intended or more desirable intermetallic compounds (see Supp. Info.). We suspect that this may be due to the relative electronegativity of Ni, compared to the tetrel in each case (see below), as well as to the higher oxophilicity of Ni, especially when compared to Pd and Pt. Also, the Ge-Pt (**3**) complex did not form an intermetallic product, which could be due to a high crystallization temperature because the TGA trace does not plateau by 600 °C, like the others do. Nonetheless, all the other heterobimetallic complexes form intermetallics when heated to at least at 400 °C. In this way, Pd_2Ge, Pd_2Sn, and PtSn intermetallic compounds are produced from the thermolysis of complexes $Cl_2Ge(\mu$-$PyS)PdPPh_3$ (**2**), $Cl_2Sn(\mu$-$PyS)PdPPh_3$ (**5**), and $Cl_2Sn(\mu$-$PyS)PtPPh_3$ (**6**), respectively (Figure 4). Notably, there are no crystalline sulfide impurities detected by XRD in any of these intermetallic products, suggesting that the sulfur from the pyridine-thiolate ligand—and up to half of the tetrel, in some cases (see below) —may be able to come

off as a volatile byproduct during thermolysis. Further, when heated to 600 °C, complex (**5**) produces Pd_3Sn_2, while complexes (**2**) and (**6**) still make the same intermetallic product that they did at 400 °C. Interestingly, many of the remaining intermetallic phases, with the exception of PtSn do not contain the same 1:1 metal-tetrel ratio that is present in the heterobimetallic precursors. Critically, elemental analysis of binary nanoparticle products such as Pd_2Sn by energy-dispersive X-ray (EDX) diffraction agrees with the new observed stoichiometry (2:1, see also XRD below). Further, the ^{119}Sn solid state (ss) NMR spectrum of Pd_2Sn nanocrystals exhibits a broad NMR signal with maximum intensity observed near the same ^{119}Sn chemical shift as that observed for Pt_3Sn and PtSn intermetallics, and is free of unreacted heterobimetallic precursor (Figure S15).[83] Therefore, we conclude that some of tetrel content in the original heterobimetallic complexes is lost as volatile material during thermal decomposition, along with the organic ligands.

To better understand why in some cases, we obtain sulfides and oxides and in other cases we obtain intermetallics, we examined the different resonance structures of the tetrel ligand, and compared them to the electronegativity difference between the metal and tetrel elements in each case (Figure 5). When the two pyridine nitrogens are negatively charged and both (thione) sulfurs are neutral, the tetrel or group 14 (IV) element (Tt) acts as a Lewis acid or Z-type ligand toward the group 10 metal (M). When the two pyridine nitrogens are neutral and both (thiolate) sulfurs are negatively charged, the Tt acts a Lewis base or L-type ligand toward M. In the intermediate case, where one each of either of the two nitrogens and either of the two sulfurs is negative and the other one is neutral, Tt may be considered as an X-type ligand toward M.[72,84]

In the cases where sulfides/oxides are obtained, specifically when starting with the Ge-Ni (**1**) and Sn-Ni (**4**) complexes, the electronegativity difference between Ni and Sn or Ge is negative, meaning that the tetrel (Tt) is more electronegative than the metal (M), and thus Tt will behave more like a Z-type ligand. In this case, the sulfur atoms more strongly donate their electron density toward the metal, strengthening the M-S interactions. In all the other cases, this electronegativity difference is positive, meaning that M is more electronegative than Tt, and thus Tt will behave more like a L-type ligand. In this case, it is the more volatile pyridine nitrogens that interact more strongly with the tetrel, rather than the sulfur atoms interacting with metal. This provides a possible framework from which we may be able to rationalize—or eat least, predict—why it is more favorable to form intermetallics, with no sulfur incorporation, in the latter case.

Interestingly, there are well defined trends in the decomposition temperatures (T_{dec}) across many of the precursors. All precursors decompose between 244 and 322 °C, with the T_{dec} increasing going down the group 10 transition metals (Figure 6a and Table 3). Also, T_{dec} increases when going from Ge to Sn complexes. A comparison between the remaining mass measured by TGA and the theoretical weight of inorganic Tt+M metals in each precursor reveals the presence of excess mass left over after thermolysis, with this excess increasing from Ni to Pt (Figure 6b). Using Raman spectroscopy, we have previously shown that this is due to the formation of graphitic carbon on the surface of the intermetallic nanoparticles.[61] Conveniently, this graphitic impurity can be very easily removed, if necessary, by plasma cleaning.[85,86] Even more importantly, the presence of such an impurity does not preclude nor impede catalytic activity—or other possible applications—of these intermetallic compounds (see below).

Based on these data together, our method of choice to routinely prepare phase-pure Pd_2Sn nanocrystals—for example—is the solid state thermolysis of $Cl_2Sn(\mu\text{-}PyS)PdPPh_3$ at 400 °C under N_2. As shown in Figure 7, this typically produces Pd_2Sn nanocrystals with a 41 ± 16 nm diameter. *d*-spacings measured for several lattice fringes, as well as multiple EDX area scans, as observed by TEM are consistent with this Pd_2Sn phase, with an overall elemental composition of 67 ± 2 atom% Pd and 33 ± 2 atom% Sn.

Table 2. Calculated structural and thermodynamic data for 10–14 heterobimetalic complexes.[a]

Compound	M-Tt Distance (Å)	M-P Distance (Å)	M-S[a] Distance (Å)	Tt-N[b] Distance (Å)	M-Ligand Binding Energy (kcal/mol)	M-P Binding Energy (kcal/mol)
$Cl_2Ge(\mu\text{-}PyS)_2NiPPh_3$ (**1**)	2.322	2.346	2.234	2.208	-794.4	-8.87
$Cl_2Ge(\mu\text{-}PyS)_2PdPPh_3$ (**2**)	2.416	2.453	2.370	2.216	-815.4	-8.40
$Cl_2Ge(\mu\text{-}PyS)_2PtPPh_3$ (**3**)	2.416	2.416	2.376	2.212	-847.2	-17.3
$Cl_2Sn(\mu\text{-}PyS)_2NiPPh_3$ (**4**)	2.463	2.339	2.238	2.313	-786.8	-9.24
$Cl_2Sn(\mu\text{-}PyS)_2PdPPh_3$ (**5**)	2.552	2.416	2.381	2.321	-809.0	-6.91
$Cl_2Sn(\mu\text{-}PyS)_2PtPPh_3$ (**6**)	2.547	2.416	2.381	2.321	-839.4	-16.7
$Cl_2Sn(\mu\text{-}PyS)_2PdPCy_3$ (**7**)	2.551	2.507	2.380	2.321	-798.8	-20.8
$Cl_2Sn(\mu\text{-}PyS)_2PdP(OPh)_3$ (**8**)	2.542	2.397	2.297	2.313	-841.7	-14.7
$Cl_2Sn(\mu\text{-}PyS)_2PdP\textit{n}Bu_3$ (**9**)	2.547	2.442	2.324	2.327	-842.3	-19.9

[a]Using density functional theory (DFT): B3LYP with hybrid exchange functional or TPSS (see Experimental). [b]Average between the two M-S bonds. [b]Average between the two Tt-N bonds.

Table 3. Thermolysis of 10–14 heterobimetallic complexes.				
Precursor	g/mol (%)	T_{dec}(°C)[a]	XRD (°C)	Res. Mass Δ[b] (%)
$Cl_2Ge(\mu\text{-}PyS)_2NiPPh_3$ (**1**)	684.82	233	Ni_2GeO_4 (600)	32
$Cl_2Ge(\mu\text{-}PyS)_2PdPPh_3$ (**2**)	732.55	244	Pd_2Ge (400, 600)	6.9
$Cl_2Ge(\mu\text{-}PyS)_2PtPPh_3$ (**3**)	821.21	291	amorph. (400, 600), Pt (800)	30
$Cl_2Sn(\mu\text{-}PyS)_2NiPPh_3$ (**4**)	730.90	266	NiS +$Ni_3Sn_2S_2$ + SnS + Ni (400, 600)	3.1
$Cl_2Sn(\mu\text{-}PyS)_2PdPPh_3$ (**5**)	778.63	294	Pd_2Sn (400), Pd_3Sn_2 (600)	10
$Cl_2Sn(\mu\text{-}PyS)_2PtPPh_3$ (**6**)	867.29	322	PtSn + Pt_3Sn[c] (400, 600)	15
$Cl_2Sn(\mu\text{-}PyS)_2PdPCy_3$ (**7**)	796.77	250	PdSn (400, 600)	14
$Cl_2Sn(\mu\text{-}PyS)_2PdP(OPh)_3$ (**8**)	826.63	260	Pd_2Sn (400), $Pd_{20}Sn_{13}$ (600)	12
$Cl(PyS)Sn(\mu\text{-}PyS)_2PdPnBu_3$ (**9**)	793.36	300	Pd_2Sn (400, 600)	-10
[a]Thermal decomposition onset from TGA/DSC. [b]Difference between mass left after TGA and mass of M + Tt: $\Delta = TGA_m^f - theo_m^{inor}$. [c]Minor impurity.				

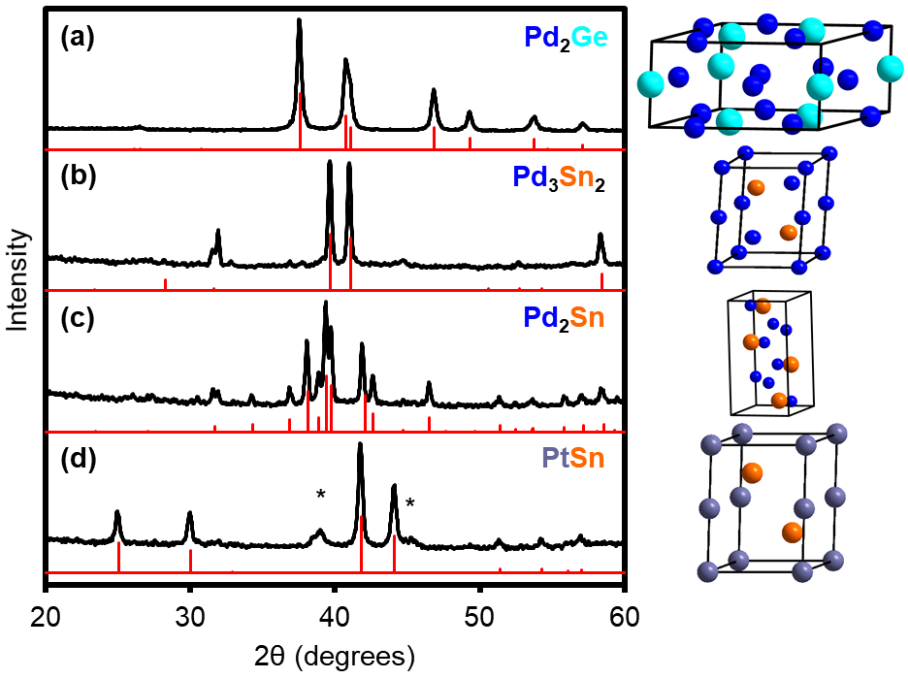

Figure 4. Selected powder XRD patterns and main product unit cells for solids obtained after the decomposition of (a) $Cl_2Ge(\mu\text{-}PyS)_2PdPPh_3$ (**2**) (600 °C), (b) $Cl_2Sn(\mu\text{-}PyS)_2PdPPh_3$ (**5**) (600 °C), (c) $Cl_2Sn(\mu\text{-}PyS)_2PdPPh_3$ (**5**) (400 °C), and (d) $Cl_2Sn(\mu\text{-}PyS)_2PtPPh_3$ (**6**) (600 °C, * = Pt_3Sn). Standard patterns are shown in red (Pd_2Ge 52052, Pd_3Sn_2 197134, Pd_2Sn 158364, PtSn 42593).[87]

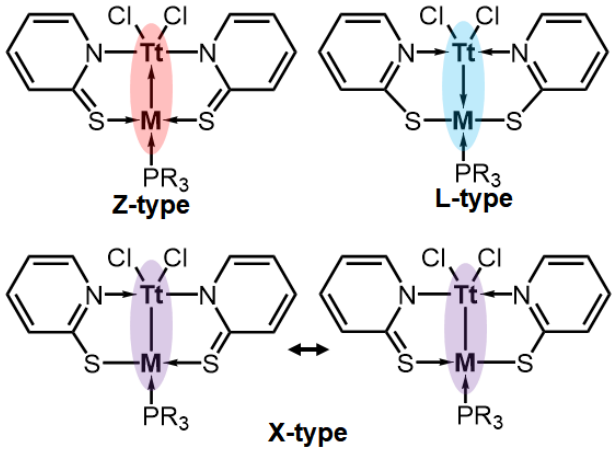

$\Delta\lambda_P$	Ni	Pd	Pt
Si	0.01	0.3	0.38
Ge	-0.1	0.19	0.27
Sn	-0.05	0.24	0.32

Figure 5. Different resonance structures for $Cl_2Tt(Pyridine\text{-}2\text{-}thiolate)_2$ show the Tt can act as a Z-, L-, or X-type ligand toward M (the phosphorous-based ligand always acts as a L-type ligand).[72,84] The chart shows the difference in Pauling electronegativities between group 10 metal (M) and tetrel (Tt) in each case, calculated as $\Delta\lambda_P = \lambda_M - \lambda_{Tt}$.

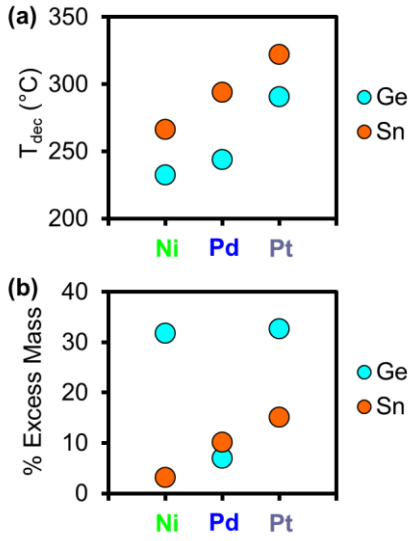

Figure 6. (a) Decomposition temperatures and (b) difference between % mass left after TGA and theoretical mass of M + Tt for different pyridine-2-thiolate heterobimetallic complexes (Tt = Ge, Sn; M = Ni, Pd, Pt).

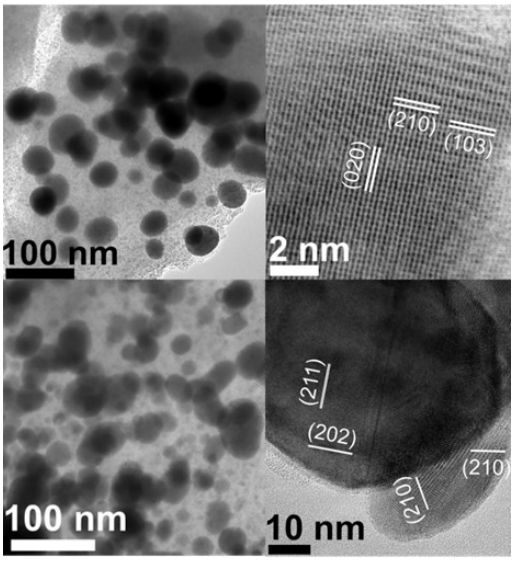

Figure 7. Representative TEM of Pd_2Sn produced by thermolysis of $Cl_2Sn(\mu\text{-}PyS)PdPPh_3$ (**5**) at 400 °C.

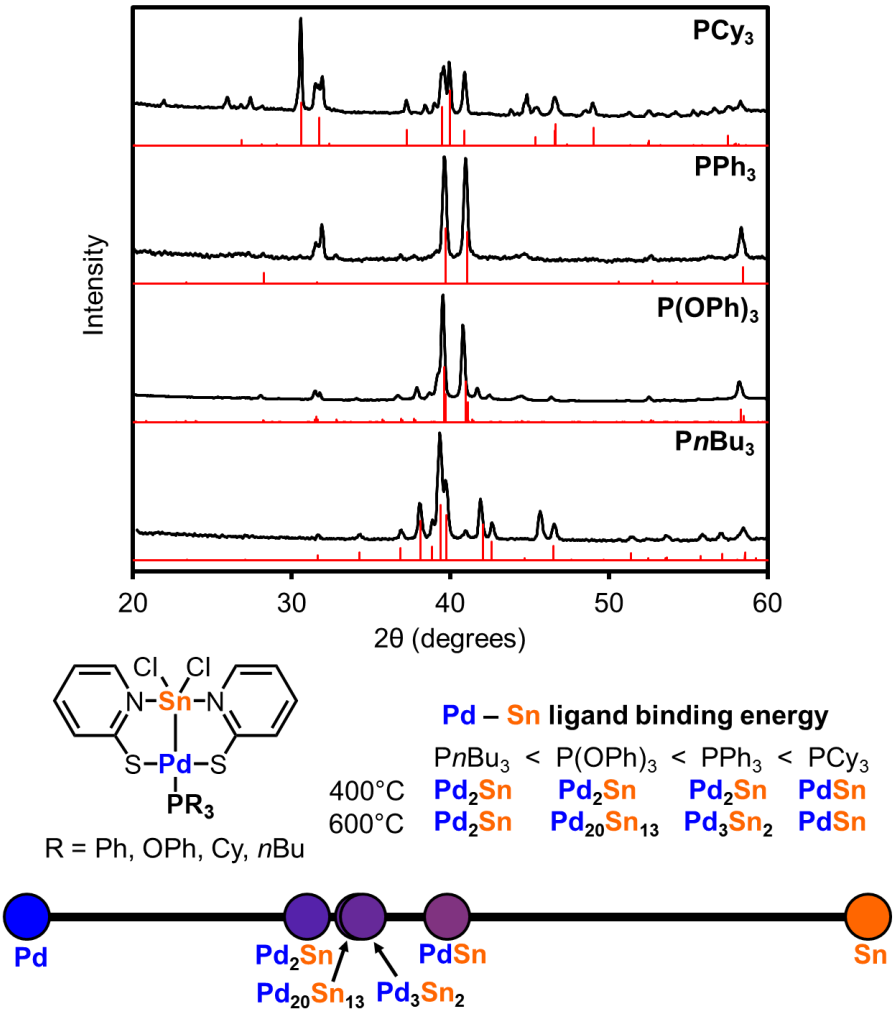

Figure 8. Formation of Pd-Sn binary phases as a function of thermolysis temperature and homoleptic phosphorus ligand.

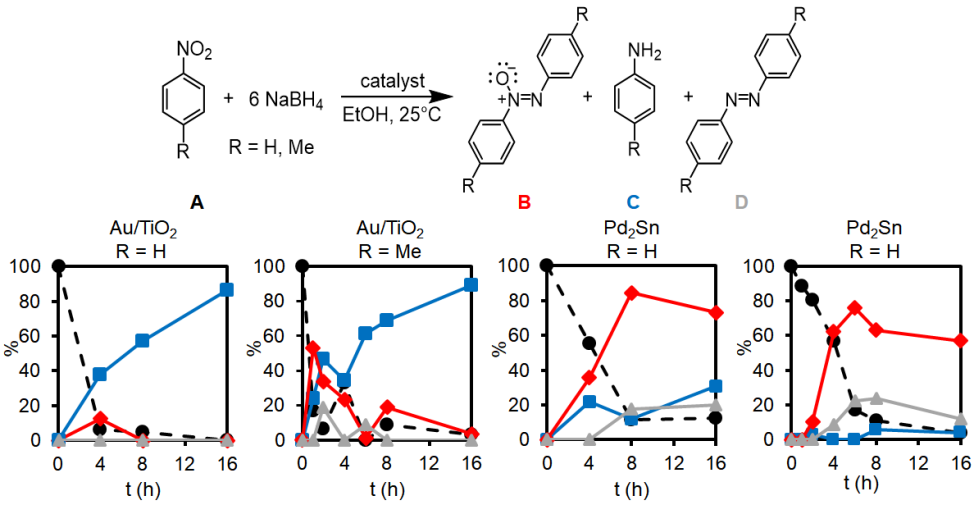

Figure 9. Reduction of nitroarenes (R = H, Me) with $NaBH_4$ in ethanol catalyzed by Pd_2Sn nanocrystals and Au/TiO_2.

Phosphine Tuning. Heterobimetallic Sn-Pd pyridine-2-thiolate complexes were synthesized with four different phosphine ligands: Triphenyl phosphine, tricyclohexylphospine, triphenylphosphite, and tri-n-butylphosphine. All four complexes were decomposed at both 400 and 600 °C under inert conditions. At 400 °C, all the complexes give Pd_2Sn as the intermetallic product, except that with PCy_3 the product is the PdSn phase. At 600 °C, PCy_3 still produces PdSn. The PPh_3 complex gives Pd_3Sn_2, the $P(OPh)_3$ complex gives $Pd_{20}Sn_{13}$, and the P*n*Bu$_3$ complex forms Pd_2Sn (Figure 8 and S14). Interestingly, the level of incorporation of Sn in the intermetallic product correlates well with our calculated metal binding energies (see above). These predict that Sn and Pd are held together increasingly more strongly in the following order: P*n*Bu$_3$ < $P(OPh)_3$ < PPh_3 < PCy_3. Thus, when PCy_3 is used, Pd and Sn are bound most strongly, resulting in the retention of the 1:1 Pd:Sn stoichiometry from precursor through thermal decomposition and into product. As the binding energy decreases, Sn is not held as strongly, and some of it is lost upon thermolysis, resulting in more Sn-deficient intermetallic products (Pd_3Sn_2, $Pd_{20}Sn_{13}$, and Pd_2Sn).

Intermetallic Catalysts and Selectivity. Because catalysis is one of the most remarkable and sought-after applications of many intermetallic compounds, we tested whether the binary intermetallic nanocrystals prepared by our heterobimetallic precursor approach could be catalytically active. Specifically, we tested Pd_2Sn against the reduction of nitro-arenes by $NaBH_4$ (Table 4). As a control, we used recently reported Au/TiO_2 heterostructures, which are known to be active catalysts for this transformation.[88] Indeed, our studies show that Pd_2Sn is also a very active catalyst in the hydrogenation of nitroarenes. However, unlike Au/TiO_2, which is known to covert nitroarenes all the way to the corresponding anilines, Pd_2Sn instead converts nitroarenes preferentially to the corresponding azoxyarenes, only (Figure 9). Normally, azoxyarenes are an intermediate in this nitro- to amino-arene (aniline) transformation. They are important and useful organic products themselves, as they can be widely used in industry as dyes, polymerization inhibitors, reducing agents, chemical stabilizers, and as important building blocks in many natural compounds and functional materials.[89,90,91,92,93] Azoxyarenes have been made through the selective reduction of nitroarenes or the selective oxidative of anilines.[94,95,96,97,98] Yet it is relatively uncommon for nitroarene reduction to stop at the azoxyarene intermediate step, making the Pd_2Sn nanocrystals made here a much more interesting catalyst than we could have first envisioned, due to their catalytic activity and unique selectivity.

Table 4. Catalytic reduction of nitroarenes.

Cat.[a]	Sub-strate[b]	Conv.[c] (%)	Prod.(s)[d]	Selec. (%)
Pd_2Sn	Nitro-benzene	91	B C D	54 23 15
Pd_2Sn	*p*-Nitro-toluene	95	B C D	70 11 15
Au/TiO_2	Nitro-benzene	100	C	100
Au/TiO_2	*p*-Nitro-toluene	97	B C	4 93
none	Nitro-benzene	9.7	n.d.	n.d.
none	*p*-Nitro-toluene	0.9	n.d.	n.d.

[a]20 mg catalyst. [b]0.1 mmol substrate in 2 mL ethanol. [c]After 16 h at 25 °C. [d]B = Azoxybenzene (R = H) or 4,4'-azoxytoluene (R = Me), C = Aniline (R = H) or *p*-toluidine (R = Me), and D = Azobenzene (R = H) or 4,4'-azotoluene (R = Me) (See Figure 9).

CONCLUSIONS

In summary, we have synthesized an expanded family of bis(pyridine-2-thiolate)based heterobimetallic complexes that contain a group 10 transition metal (Ni, Pd, or Pt) bonded to a tetrel element (Ge or Sn). Upon thermal decomposition, these heterobimetallic complexes form a

variety of group 10-14 binary intermetallics. To better understand these precursors, we performed DFT calculations to identify geometry trends and to understand the behavior and binding of the Tt-based pyridine-2-thiolate ligand. We also discovered that different Sn-Pd intermetallic phases could be produced by changing the monodentate phosphorous ligand, and that the Sn:Pd ratio in the binary products correlates to how well the Sn ligand binds to Pd. To demonstrate the utility of the intermetallic binaries made in this way, we used Pd_2Sn as a catalyst for the hydrogenation of nitroarenes. Compared to typical metallic catalysts, which usually produce the corresponding anilines, intermetallic Pd_2Sn nanoparticles made through our heterobimetallic precursor approach are selective to the intermediate azoxyarenes. Using this group 10–14 family of heterobimetallic complexes, we were able to show a versatile approach toward the synthesis of intermetallic nanocatalysts with unique selectivity, underscoring how molecular organometallic complexes can be utilized and developed toward the synthesis of materials with interesting applications.

EXPERIMENTAL

Materials. Bis(1,5-cyclooctadiene)Ni ($Ni(COD)_2$, 98+%), tetrakis(triphenylphosphine)platinum ($Pt(PPh_3)_4$, 98%), bis(dibenzylideneacetone)palladium ($Pd(dba)_2$), triphenylphosphine (PPh_3, 99%), triphenylphosphite ($P(OPh)_3$, 97%), tri-n-butyl phosphine ($PnBu_3$, 99%), tricyclohexylphosphine (PCy_3, 97%), and gold nanoparticles on titania (1% Au/TiO_2) were purchased from Strem. Tetrahydrofuran (THF, 99.9%, extra dry, anhydrous), sodium borohydride powder ($NaBH_4$, 98+%) and 4-nitrotoluene (99%) were purchased from Acros Organics. Nitrobenzene (99%) was purchased from Oakwood Chemical. Diethyl ether (Et_2O, 99.7+%, anhydrous) was purchased from MilliporeSigma. $CDCl_3$, DMSO-d_6, and CD_2Cl_2 were purchased from Cambridge Isotope Labs. The tetrel-based ligands $Cl_2Sn(PyS)_2$ and $Cl_2Ge(PyS)_2$, as well as the heterobimetallic complexes $Cl_2Ge(\mu\text{-}PyS)_2PdPPh_3$, $Cl_2Sn(\mu\text{-}PyS)_2NiPPh3$, $Cl_2Sn(\mu\text{-}PyS)_2PdPPh_3$, $Cl_2Sn(\mu\text{-}PyS)_2PtPPh_3$, and $Cl_2Sn(\mu\text{-}PyS)_2PdCy_3$ were synthesized according to literature procedures.[72,81,99]

Precursor Synthesis. The new heterobimetallic complexes $Cl_2Ge(\mu\text{-}PyS)_2NiPPh_3$, $Cl_2Ge(\mu\text{-}PyS)_2PtPPh_3$, $Cl_2Sn(\mu\text{-}PyS)_2PdP(OPh)_3$, and $Cl_2Sn(\mu\text{-}PyS)_2PdPnBu_3$ were synthesized under a nitrogen atmosphere as follows. *$Cl_2Ge(\mu\text{-}PyS)_2NiPPh_3$* (**1**). $Cl_2Ge(PyS)_2$ (100 mg, 0.275 mmol) and PPh_3 (72.1 mg, 0.275 mmol) were added to a solution of $Ni(COD)_2$ (75.6 mg, 0.275 mmol) in THF (5 mL). After stirring for 2 h at R.T., the solution was filtered and slowly layered with 5 mL of Et_2O. Brownish-yellow X-ray quality crystals were formed within a day, isolated by decantation, washed with diethyl ether, and dried under vacuum. Yield: 29 mg (15 %). T_{dec} = 233 °C. *$Cl_2Ge(\mu\text{-}PyS)_2PtPPh_3$* (**3**). $Cl_2Ge(PyS)_2$ (60 mg, 0.165 mmol) was added to a solution of $Pt(PPh_3)_4$ (200 mg, 0.161 mmol) in THF (4 mL). After 1 h stirring at 50 °C, the solution was filtered. Orange single crystals suitable for X-ray diffraction were obtained by slow vapor diffusion of Et_2O for 3 days at R.T. Yield: 35 mg (26 %). ^{1}H NMR ($CDCl_3$, 21 °C): δ = 6.99 (m, 2H, C5H PyS), 7.55 (m, 2H, C4H PyS), 7.40–7.50 (mm, 9H, $Ph_{meta,para}$), 7.69 (m, 2H, C3H PyS), 7.85 (mm, 6H, Ph_{ortho}), 8.31 (m, 2H, C6H PyS). ^{13}C{H} NMR ($CDCl_3$, 21 °C): δ = 126.0 (C5 PyS), 128.4 (d, OPh_{ortho}), 131.3 (C3 PyS), 134.4 (d, OPh_{meta}), 135.0 (br, OPh_{ipso}), 138.6 (br, OPh_{para}), 143.8 (C4 PyS), 150.7 (C6 PyS), 160.3 ppm (C2 PyS). ^{31}P{^{1}H} NMR ($CDCl_3$, 21 °C): δ 10.7 (J^{195}Pt-^{31}P = 3171 Hz). ^{195}Pt{^{1}H} NMR ($CDCl_3$, 21 °C): δ -4961 (J^{31}P-^{195}Pt = 3173 Hz). Anal. Found (calcd): C, 40.95 (41.26), H, 2.82 (2.69), N, 3.41 (3.66). T_{dec} = 291 °C. *$Cl_2Sn(\mu\text{-}PyS)_2PdP(OPh)_3$* (**8**). $Cl_2Sn(PyS)_2$ (100 mg, 0.244 mmol) and $P(OPh)_3$ (0.1 mL, 0.381 mmol) were added to a solution of $Pd(dba)_2$ (140 mg, 0.243 mmol) in THF (5 mL). The solution was stirred for 1 h at R.T. and filtered. Red crystals suitable for X-ray diffraction were obtained by slow vapor diffusion of Et_2O for 2 days at R.T. Yield: 159 mg (79 %). ^{1}H NMR ($CDCl_3$, 21 °C): δ = 7.00 (m, 2H, C5H PyS), 7.10–7.21 (mm, 15H, $OPh_{ortho,meta,para}$), 7.39 (m, 2H, C4H PyS), 7.65 (m, 2H, C3H PyS), 8.47 (m, 2H, C6H PyS). ^{13}C{H} NMR ($CDCl_3$, 21 °C): δ = 118.6 (C5 PyS), 120.9 (d, OPh_{meta}), 124.8 (br, OPh_{ipso}), 125.1 (C3 PyS), 129.9 (d, OPh_{ortho}), 138.1 (C6 PyS), 145.6 (C4 PyS), 151.3 (br, OPh_{para}), 157.6 ppm (C2 PyS). ^{31}P{^{1}H} NMR ($CDCl_3$, 21 °C): δ 127.8 (br). ^{31}P{^{1}H} ssNMR (21 °C): δ 127.8 (br). T_{dec} = 260 °C. *$Cl_2Sn(\mu\text{-}PyS)_2PdPnBu_3$*. $Cl_2Sn(PyS)_2$ (**9**). (100 mg, 0.244 mmol) and $PnBu_3$ (0.1 mL, 0.405 mmol) were added to a solution of $Pd(dba)_2$ (140 mg, 0.243 mmol) in THF (5 mL). The solution was stirred for 2 h at R.T. and filtered. Orange X-ray quality crystals were obtained by slow solvent evaporation. Yield: 90 mg (47 %). ^{1}H NMR (DMSO-d_6, 21 °C): δ = 7.37 (m, 3H, C5H PyS), 7.47 (m, 3H, C4H PyS), 7.80 (m, 3H, C3H PyS), 8.41 (m, 3H, C6H PyS), 1.10-1.60 (18H, $C3CH_2CH_2CH_2$, $PnBu_3$), 0.87 (m, 9H, $C4CH_3$ $PnBu_3$). ^{13}C{H} NMR (DMSO-d_6, 21 °C): δ = 125.7 (C5 PyS), 128.8 (C3 PyS), 130.5 (C6 PyS), 134.7 (C4 PyS), 142.8 (C2 PyS), 25.8 ($C1CH_2$ $PnBu_3$), 23.4 ($C2CH_2$ $PnBu_3$), 13.6 ($C3CH_2$ $PnBu_3$), 13.2 ($C4CH_3$ $PnBu_3$). ^{31}P{^{1}H} NMR (DMSO-d_6, 21 °C): δ 36.4 (s). T_{dec} = 300 °C.

Calculations. All molecules were constructed using GaussView and optimized with the Gaussian 09 package.[100] The popular B3LYP with hybrid exchange functional[79] was used for all geometry optimization and frequency calculations. Additional calculations were performed on the $Cl_2Sn(\mu\text{-}PyS)_2PdPPh_3$ complex using the TPSS functional,[80] in order to compare the results to the B3LYP DFT functional. One of the biggest deficiencies in DFT methods is the long-range dispersion correction in B3LYP, which is 1.05 and rather big compared with other DFT functionals.[101] Compared to other density functionals, TPSS generally gives excellent results for a wide range of systems and properties, correcting overestimated PKZB (Perdew–Kurth–Zupan–Blaha) bond distances in molecules, hydrogen-bonded complexes, and ionic solids. The LANL2DZ basis set with Effective Core Potentials (ECP) was used for the metal (Ni, Pd, Pt) and tetrel (Ge and Sn) elements,[102,103] and the 6-31G(d,p) basis set for the rest of elements,[104,105] for the initial geometry optimization. Other comparisons were made with the Stuttgart ESC 1997 ECP basis set for Pd,[106] Stuttgart ELC ECP basis set for Sn[107], cc-pvDZ-PP basis set for Pd and Sn,[108,109,110] and aug-cc-pvTZ-PP Diffuse basis set for Pd and Sn.[108,109,110] (can Hua Jun please check) The basis sets and inputs were adapted from the "Basis Set Exchange" website maintained by The Molecular Sciences Software Institute.[111] All structures were fully optimized, and frequency analyses were performed

to ensure a minimum was achieved, which had zero imaginary vibrational frequencies as derived from a vibrational frequency analysis. The thermodynamic parameters of the reaction such as zero-point corrected energy (ΔEZPE), enthalpies (ΔH°), and Gibbs Free energies (ΔG°), were calculated at 298.15 K and 1 atm.

Precursor Thermolysis. Thermogravimetric analysis and differential scanning calorimetry (TGA-DSC) were measured on a Netzsch DSC/TGA (STA449 F1). For each experiment, 5-10 mg of precursor were placed into an aluminum crucible, which was then inserted into the furnace of the TGA-DSC in an Ar atmosphere. After an initial 5 min isothermal step near R.T., the temperature was increased to 600 °C at a ramp rate of 10 °C/min. After cooling to room temperature, the remaining solid was removed and analyzed by power x-ray diffraction (XRD).

Characterization. *Structural: Single crystal X-ray diffraction* (XRD) measurements were performed at 173(2) K using a Bruker APEX–II CCD area detector diffractometer (Cu-K_α radiation, λ = 1.54178 Å) for $Cl_2Ge(\mu\text{-}PyS)_2NiPPh_3$ (**1**) and $Cl_2Ge(\mu\text{-}PyS)_2PtPPh_3$ (**3**). For $Cl_2Sn(\mu\text{-}PyS)_2PdP(OPh)_3$ (**8**) and *$Cl_2Sn(\mu$-$PyS)_2PdP$nBu_3*. $Cl_2Sn(PyS)_2$ (**9**), a Bruker Venture D8 diffractometer with a Photon CMOS detector was used at 173(2) K (Mo-K_α radiation, λ = 0.71073 Å). *Powder XRD* was collected on a Rigaku Ultima IV diffractometer using a Cu Kα radiation source (40 kV, 44 mA). Each sample was prepared by smearing 2-5 mg of powder onto a backgroundless quartz slide. *Spectroscopy. NMR* spectroscopy was recorded on a Bruker Avance III 600 spectrometer at room temperature at 600.39 MHz for ^{1}H, 150.97 MHz for ^{13}C, 243.04 MHz for ^{31}P, 223.89 MHz for ^{119}Sn, and 129.06 MHz for ^{195}Pt. ^{1}H and ^{13}C NMR shifts are given in ppm and referenced to residual protonated solvent signals. ^{31}P, ^{119}Sn, and ^{195}Pt NMR shifts are given in ppm and referenced to the ^{1}H spectrum residual solvent peaks using indirect referencing.[112]

Intermetallic Catalysis. For each reaction, the nitroarene substrate (nitrobenzene or 4-nitrotoluene, 0.1 mmol) was added to a 5 mL vial, followed by the addition of ethanol (2 mL), catalyst (Au/TiO_2 or Pd_2Sn, 10-20 mg), and $NaBH_4$ (0.6 mmol). The reaction was stirred for 16 h. During the reaction, small aliquots (~0.2 mL) were taken at specific intervals, filtered, and diluted for analysis by gas chromatography-mass spectroscopy (GCMS).

ASSOCIATED CONTENT

Supporting Information. Additional data including computational data (frontier orbitals), crystallographic data (cif files), full thermal analysis and powder XRD measurements, particle size histogram for Pd_2Sn, and solid-state (ss) NMR measurements for $Cl_2Sn(\mu\text{-}PyS)_2PdP(OPh)_3$ (**5**) and Pd_2Sn. This material is available free of charge via the Internet at http://pubs.acs.org.

AUTHOR INFORMATION

Corresponding Author

* vela@iastate.edu

Notes

The authors declare no competing financial interests.

ACKNOWLEDGMENT

J.V. thanks the U.S. National Science Foundation for a grant from the Division of Chemistry, Macromolecular, Supramolecular, and Nanochemistry Program (1905066). Y.C., R.W.D. and A.J.R. were supported by the U.S. Department of Energy (DOE), Office of Science, Basic Energy Sciences, Materials Science and Engineering Division. The Ames Laboratory is operated for the U.S. DOE by Iowa State University under contract #DE-AC02-07CH11358. We thank Arkady Ellern and Amrit Venkatesh for assistance with single crystal X-ray diffraction and solid state NMR, respectively.

REFERENCES

[1] Furukawa, S.; Komatsu, T. Intermetallic Compounds: Promising Inorganic Materials for Well-Structured and Electronically Modified Reaction Environments for Efficient Catalysis. *ACS Catal.* **2017**, *7*, 735–765.

[2] Yan, Y.; Du, J. S.; Gilroy, K. D.; Yang, D.; Xia, Y.; Zhang, H. Intermetallic Nanocrystals: Syntheses and Catalytic Applications. *Adv. Mater.* **2017**, *29*, 1605997.

[3] Gilroy, K. D.; Ruditskiy, A.; Peng, H.-C.; Qin, D.; Xia, Y. Bimetallic Nanocrystals: Syntheses, Properties, and Applications. *Chem. Rev.* **2016**, *116*, 10414–10472.

[4] Jana, S. Advances in Nanoscale Alloys and Intermetallics: Low Temperature Solution Chemistry Synthesis and Application in Catalysis. *Dalton Trans.* **2015**, *44,* 18692–18717.

[5] Marakatti, V. S.; Peter, S. C. Synthetically Tuned Electronic and Geometrical Properties of Intermetallic Compounds as Effective Heterogeneous Catalysts. *Prog. Solid State Chem.* **2018**, *52*, 1–30.

[6] Bauer, J. C.; Chen, X.; Liu, Q.; Phanab, T.-H.; Schaak, R. E. Converting Nanocrystalline Metals into Alloys and Intermetallic Compounds for Applications in Catalysis. *J. Mater. Chem.* **2008**, *18*, 275–282.

[7] Wang, X.; Stöver, J.; Zielasek, V.; Altmann, L.; Thiel, K.; Al-Shamery, K.; Bäumer, M.; Borchert, H.; Parisi, J.; Kolny-Olesiak, J. Colloidal Synthesis and Structural Control of PtSn Bimetallic Nanoparticles. *Langmuir* **2011**, *27*, 11052–11061.

[8] Cortright, R. D.; Dumesic, J. A. L-Zeolite-Supported Platinum and Platinum/Tin Catalysts for Isobutane Dehydrogenation. *Appl. Catal., A* **1995**, *129*, 101–115.

[9] Bariås, O. A.; Holmen, A.; Blekkan, E. A.; Propane Dehydrogenation over Supported Pt and Pt–Sn Catalysts: Catalyst Preparation, Characterization, and Activity Measurements. *J. Catal.* **1996**, *158*, 1–12.

[10] Kaylor, N.; Davis, R. J. Propane Dehydrogenation over Supported Pt-Sn Nanoparticles. *J. Catal.* **2018**, *367*, 181–193.

[11] Hauser, A. W.; Horn, P. R.; Head-Gordon, M.; Bell, A. T. A Systematic Study on Pt Based, Subnanometer-sized Alloy Cluster Catalysts for Alkane Dehydrogenation: Effects of Intermetallic Interaction. *Phys. Chem. Chem. Phys.* **2016**, *18*, 10906–10917.

[12] Deng, L.; Miura, H.; Shishido, T.; Hosokawa, S.; Teramura, K.; Tanaka, T. Dehydrogenation of Propane over Silica-Supported Platinum–Tin Catalysts Prepared by Direct Reduction: Effects of

Tin/Platinum Ratio and Reduction Temperature. *ChemCatChem* **2014**, *6*, 2680–2691.
[13] Furukawa, S.; Tamura, A.; Ozawa, K.; Komatsu, T. Catalytic Properties of Pt-based Intermetallic Compounds in Dehydrogenation of Cyclohexane and *n*-Butane. *Appl. Catal., A* **2014**, *469*, 300–305.
[14] Nykänen, L.; Honkala, K. Selectivity in Propene Dehydrogenation on Pt and Pt_3Sn Surfaces from First Principles. *ACS Catal.* **2013**, *3*, 3026–3030.
[15] Lobera, M. P.; Téllez, C.; Herguido, J.; Menéndez, M. Transient Kinetic Modelling of Propane Dehydrogenation over a Pt–Sn–K/Al_2O_3 Catalyst. *Appl. Catal., A* **2008**, *349*, 156–164.
[16] Nawaz, Z. Tang, X.; Zhang, Q.; Wang, D.; Fei, W. SAPO-34 Supported Pt–Sn-based Novel Catalyst for Propane Dehydrogenation to Propylene. *Catal. Commun.* **2009**, *10*, 1925–1930.
[17] Kumar, M. S.; Chen, D.; Holmen, A.; Walmsley, J. C. Dehydrogenation of Propane over Pt-SBA-15 and Pt-Sn-SBA-15: Effect of Sn on the Dispersion of Pt and Catalytic Behavior. *Catal. Today* **2009**, *142*, 17–23.
[18] Pisduangdaw, S.; Panpranot, J.; Methastidsook, C.; Chaisuk, C.; Faungnawakij, K.; Praserthdam, P.; Mekasuwandumrong, O. Characteristics and Catalytic Properties of Pt–Sn/Al_2O_3 Nanoparticles Synthesized by One-step Flame Spray Pyrolysis in the Dehydrogenation of Propane. *Appl. Catal., A* **2009**, *370*, 1–6.
[19] Sahebdelfar, S.; Zangeneh, F. T. Dehydrogenation of Propane to Propylene Over Pt-Sn/Al_2O_3 Catalysts: The Influence of Operating Conditions on Product Selectivity. *Iran J. Chem. Chem. Eng.* **2010**, *7*, 51–57.
[20] Yang, M.-L.; Zhu, Y.-A.; Zhou, X.-G.; Sui, Z.-J.; Chen, D. First-Principles Calculations of Propane Dehydrogenation over PtSn Catalysts. *ACS Catal.* **2012**, *2*, 1247–1258.
[21] Vandichel, M.; Moscu, A.; Grönbeck, H. Catalysis at the Rim: A Mechanism for Low Temperature CO Oxidation over Pt_3Sn. *ACS Catal.* **2017**, *7*, 7431–7441.
[22] Tripković, D.; Stevanović, S.; Gavrilović, A.; Rogan, J.; Lačnjevac, U.; Kravić, T.; Jovanović, V. M. The Role of SnO_2 on Electrocatalytic Activity of PtSn Catalysts. *Electrocatalysis* **2018**, *9*, 76–85.
[23] Michalak, W. D.; Krier, J. M.; Alayoglu, S.; Shin, J.-Y.; An, K.; Komvopoulos, K.; Liu, Z.; Somorjai, G. A. CO Oxidation on PtSn Nanoparticle Catalysts Occurs at the Interface of Pt and Sn Oxide Domains Formed Under Reaction Conditions. *J. Catal.* **2014**, *312*, 17–25.
[24] Liu, Y.; Li, D.; Stamenkovic, V. R.; Soled, S.; Henao, J. D.; Sun, S. Synthesis of Pt_3Sn Alloy Nanoparticles and Their Catalysis for Electro-Oxidation of CO and Methanol. *ACS Catal.* **2011**, *1*, 1719–1723.
[25] Wei, Z.; Guo, H.; Tang, Z. Methanol Electro-Oxidation on Platinum and Platinum-Tin Alloy Catalysts Dispersed on Active Carbon. *J. Power Sources* **1996**, *58*, 239–242.
[26] Kumar, M. S.; Chen, D.; Holmen, A.; Walmsley, J. C. Dehydrogenation of Propane over Pt-SBA-15 and Pt-Sn-SBA-15: Effect of Sn on the Dispersion of Pt and Catalytic Behavior. *Catal. Today* **2009**, *142*, 17–23.
[27] Gerceker, D.; Motagamwala, A. H.; Rivera-Dones, K. R.; Miller, J. B.; Huber, G. W. Mavrikakis, M.; Dumesic, J. A. Methane Conversion to Ethylene and Aromatics on PtSn Catalysts. *ACS Catal.* **2017**, *7*, 2088–2100.
[28] Komatsu, T.; Ikenaga, H. Dehydroisomerization of Butane into Isobutene on Pt–Sn Intermetallic Compounds Supported on H-SAPO-11. *J. Catal.* **2006**, *241*, 426–434.
[29] Ding, J.; Bu, L.; Zhang, N.; Yao, J.; Huang, Y.; Huang, X. Facile Synthesis of Ultrathin Bimetallic PtSn Wavy Nanowires by Nanoparticle Attachment as Enhanced Hydrogenation Catalysts. *Chem. Eur. J.* **2015**, *21*, 3901–3905.
[30] Pei, Y.; Qi, Z.; Goh, T. W.; Wang, L.-L.; Maligal-Ganesh, R. V.; MacMurdo, H. L.; Zhang, S.; Xiao, C.; Li, X.; Tao, F.; Johnson, D. D.; Huang, W. Intermetallic Structures with Atomic Precision for Selective Hydrogenation of Nitroarenes. *J. Catal.* **2017**, *356*, 307–314.
[31] Maligal-Ganesh, R. V.; Xiao, C.; Goh, T. W.; Wang, L.-L.; Gustafson, J.; Pei, Y. Qi, Z.; Johnson, D. D.; Zhang, S.; Tao, F.; Huang, W. A Ship-in-a-Bottle Strategy to Synthesize Encapsulated Intermetallic Nanoparticle Catalysts: Exemplified for Furfural Hydrogenation. *ACS Catal.* **2016**, *6*, 1754–1763.
[32] Zhang, Z.; Ge, J.; Ma, L.; Liao, J.; Lu, T.; Xing, W. Highly Active Carbon-supported PdSn Catalysts for Formic Acid Electrooxidation. *Fuel Cells* **2009**, *9*, 114–120.
[33] Liu, Z.; Zhang, X. Carbon-supported PdSn Nanoparticles as Catalysts for Formic Acid Oxidation. *Electrochem. Commun.* **2009**, *11*, 1667–1670.
[34] Luo, Z. Lu, J.; Flox, C.; Nafira, R.; Genç, A.; Arbiol, J.; Llorca, J.; Ibáñez, M.; Morante, J. R.; Cabot, A. Pd_2Sn [010] Nanorods as a Highly Active and Stable Ethanol Oxidation Catalyst. *J. Mater. Chem. A* **2016**, *4*, 16706.
[35] Luo, Z.; Ibáñez, M.; Antolín, A. M.; Genç, A.; Shavel, A.; Contreras, S.; Medina, F.; Arbiol, J.; Cabot, A. Size and Aspect Ratio Control of Pd_2Sn Nanorods and Their Water Denitration Properties. *Langmuir* **2015**, *31*, 3952–3957.
[36] Onda, A.; Komatzu, T.; Yashima, T. Characterization and Catalytic Properties of Ni-Sn Intermetallic Compounds in Acetylene Hydrogenation. *Phys. Chem. Chem. Phys.* **2000**, *2*, 2999–3005.
[37] Xu, Y.; Jin, H.; Hirano, T.; Matsushita, Y.; Zhang, J. Characterization of Ni_3Sn Intermetallic Nanoparticles Fabricated by Thermal Plasma Process and Catalytic Properties for Methanol Decomposition. *Sci. Technol. Adv. Mater.* **2019**, *20*, 622–631.
[38] Chen, J.-Y.; Jheng, S.-L.; Tuan, H.-Y. Synthesis of Nickel Germanide ($Ge_{12}Ni_{19}$) Nanoparticles for Durable Hydrogen Evolution Reaction in Acid Solutions. *Nanoscale* **2018**, *10*, 11072–11078.
[39] Lim, S.-C.; Hsiao, M.-C.; Lu, M.-D.; Tung, J.-L.; Tuan, H.-Y. Synthesis of Germanium–Platinum Nanoparticles as High-Performance Catalysts for Spray-Deposited Large-Area Dye-Sensitized Solar Cells (DSSC) and the Hydrogen Evolution Reaction (HER). *Nanoscale* **2018**, *10*, 16657–16666.
[40] Sarkar, S.; Jana, R.; Suchitra, Waghmare, U. V.; Kuppan, B.; Sampath, S.; Peter, S. C. Ordered Pd_2Ge Intermetallic Nanoparticles as Highly Efficient and Robust Catalyst for Ethanol Oxidation. *Chem. Mater.* **2015**, *27*, 7459–7467.
[41] Chen, X.; Zhao, A.; Shao, Z.; Li, C.; Williams, C. T.; Liang, C. Synthesis and Catalytic Properties for Phenylacetylene Hydrogenation of Silicide Modified Nickel Catalysts. *J. Phys. Chem. C* **2010**, *114*, 16525–16533.
[42] Chen, X.; Li, M.; Guan, J.; Wang, X.; Williams, C. T.; Liang, C. Nickel–Silicon Intermetallics with Enhanced Selectivity in Hydrogenation Reactions of Cinnamaldehyde and Phenylacetylene. *Ind. Eng. Chem. Res.* **2012**, *51*, 3604–3611.
[43] Dong, Z.; Wang, T.; Zhao, J.; Fu, T.; Guo, X.; Peng, L.; Zhao, B.; Xue, N.; Ding, W.; Xie, Z. Ni-Silicides Nanoparticles as Substitute for Noble Metals for Hydrogenation of Nitrobenzene to *p*-Aminophenol in Sulfuric Acid. *Appl. Catal., A* **2016**, *520*, 151–156.
[44] Ryabchuk, P.; Agostini, G.; Pohl, M.-M.; Lund, H.; Agapova, A.; Junge, H.; Junge, K.; Beller, M. Intermetallic Nickel Silicide Nanocatalyst—A Non-Noble Metal–based General Hydrogenation Catalyst. *Sci. Adv.* **2018**, *4*, eaat0761.
[45] Zhang, L.; Chen, X.; Peng, Z.; Liang, C. Chemoselective Hydrogenation of Cinnamaldehyde over MOFs-derived M_2Si@C (M = Fe, Co, Ni) Silicides Catalysts. *Mol. Catal.* **2018**, *449*, 14–24.
[46] McEnaney, J. M.; Schaak, R. E. Solution Synthesis of Metal Silicide Nanoparticles. *Inorg. Chem.* **2015**, *54*, 707–709.
[47] Yang, K.; Chen, X.; Wang, L.; Zhang, L.; Jin, S.; Liang, C. SBA-15-Supported Metal Silicides Prepared by Chemical Vapor Deposition as Efficient Catalysts Towards the Semihydrogenation of Phenylacetylene. *ChemCatChem* **2017**, *9*, 1337–1342.
[48] Lu, Y.; Li, J.; Tada, T.; Toda, Y.; Ueda, S.; Yokoyama, T.; Kitano, M.; Hosono, H. Water Durable Electride Y_5Si_3: Electronic Structure and Catalytic Activity for Ammonia Synthesis. *J. Am. Chem. Soc.* **2016**, *138*, 3970–3973.
[49] Wu, Y.; Gong, Y.; Inoshita, T.; Fredrickson, D. C.; Wang, J.; Lu, Y.; Kitano, M.; Hosono, H. Tiered Electron Anions in Multiple Voids of LaScSi and Their Applications to Ammonia Synthesis. *Adv. Mater.* **2017**, *29*, 1700924.
[50] Lu, Y.; Li, J.; Ye, T.-N.; Kobayashi, Y.; Sasase, M.; Kitano, M.; Hosono, H. Synthesis of Rare-Earth-Based Metallic Electride Nano-

particles and Their Catalytic Applications to Selective Hydrogenation and Ammonia Synthesis. *ACS Catal.* **2018**, *8*, 11054–11058.
[51] Gong, Y.; Wu, J.; Kitano, M.; Wang, J.; Ye, T.-N.; Li, J.; Kobayashi, Y.; Kishida, K.; Abe, H.; Niwa, Y.; Yang, H.; Tada, T.; Hosono, H. Ternary Intermetallic LaCoSi as a Catalyst for N_2 Activation. *Nat. Catal.* **2018**, *1*, 178–185.
[52] Mizoguchi, H.; Park, S.-W.; Kishida, K.; Kitano, M.; Kim, J.; Sasase, M.; Honda, T.; Ikeda, K.; Otomo, T.; Hosono, H. Zeolitic Intermetallics: LnNiSi (Ln = La–Nd). *J. Am. Chem. Soc.* **2019**, *141*, 3376–3379.
[53] Kieslich, G.; Birkel, C. S.; Stewart, A.; Kolb, U.; Tremel, W. Solution Synthesis of Nanoparticular Binary Transition Metal Antimonides. *Inorg. Chem.* **2011**, *50*, 6938–6943.
[54] Heise, M.; Chang, J.-H.; Schönemann, R.; Herrmannsdörfer, T.; Wosnitza, J.; Ruck, M. Full Access to Nanoscale Bismuth-Palladium Intermetallics by Low-Temperature Syntheses. *Chem. Mater.* **2014**, *26*, 5640–5646.
[55] Xie, J.; Zhao, X. B.; Yu, H. M.; Qi, H.; Cao, G. S.; Tu, J. P. Low Temperature Solvothermal Synthesis of Nanosized NiSb as a Li-ion Battery Anode Material. *J Alloys Compd.* **2007**, *441*, 231–235.
[56] Teichert, J.; Heise, M.; Chang, J.-H.; Ruck, M. Refinement of the Microwave-Assisted Polyol Process for the Low-Temperature Synthesis of Intermetallic Nanoparticles. *Eur. J. Inorg. Chem.* **2017**, 4930–4938.
[57] Cable, R. E.; Schaak, R. E. Low-Temperature Solution Synthesis of Nanocrystalline Binary Intermetallic Compounds Using the Polyol Process. *Chem. Mater.* **2005**, *17*, 6835–6841.
[58] Chou, N. H.; Schaak, R. E. Shape-Controlled Conversion of β-Sn Nanocrystals into Intermetallic M-Sn (M = Fe, Co, Ni, Pd) Nanocrystals. *J. Am. Chem. Soc.* **2007**, *129*, 7339–7345.
[59] Henderson, N. L.; Shaak, R. E. Low Temperature Solution-Mediated Synthesis of Polycrystalline Intermetallic Compounds from Bulk Metal Powders. *Chem. Mater.* **2008**, *20*, 3212–3217.
[60] Henderson, N. L.; Straesser, M. D.; Sabato, P. E.; Shaak, R. E. Toward Green Metallurgy: Low-Temperature Solution Synthesis of Bulk-Scale Intermetallic Compounds in Edible Plant and Seed Oils. *Green Chem.* **2009**, *11*, 974–978.
[61] Daniels, C. L.; Mendivelso-Perez, D. L.; Rosales, B. A.; You, D.; Sahu, S.; Jones, J. S.; Smith, E. A.; Gabbaï, F. P.; Vela, J. Heterobimetallic Single-Source Precursors: A Springboard to the Synthesis of Binary Intermetallics. *ACS Omega* **2019**, *4*, 5197–5203.
[62] Malik, M. A.; Afzaal, M.; O'Brien, P. Precursor Chemistry for Main Group Elements in Semiconducting Materials. *Chem. Rev*. **2010**, *110*, 4417–4446.
[63] Cowley, A. H.; Jones, R. A. The Single-Source Precursor Concept. A Case Study of Gallium Arsenide. *Polyhedron*. **1994**, *13*, 1149–1157.
[64] Buhro, W. E. Progress in Molecular Precursors for Electronic Materials. *Adv. Mater. Opt. Electron.* **1996,** *6,* 175–184.
[65] Wooten, A.; Werder, D.; Williams, D.; Casson, J.; Hollingsworth, J. A. Solution-Liquid-Solid Growth of Ternary Cu-In-Se Semiconductor Nanowires from Multiple- and Single-Source Precursors. *J. Am. Chem. Soc.* **2009**, *131*, 16177–16188.
[66] Trindale, T.; O'Brien P. Synthesis of CdS and CdSe Nanocrystallites Using a Novel Single-Molecule Precursors Approach. *Chem. Mater.* **1997**, *9*, 523–530.
[67] Dhanapala, D. B.; Munasinghe, H. N.; Suescun, L.; Rabuffetti, F. A. Bimetallic Trifluoroacetates as Single-Source Precursors for Alkali–Manganese Fluoroperovskites. *Inorg. Chem.* **2017,** 56, 13311–13320.
[68] Buhro, W. E. Metallo-Organic Routes to Phosphide Semiconductors. *Polyhedron* **1994**, *13*, 1131–1148.
[69] McElwee-White, L. Design of Precursors for the CVD of Inorganic Thin Films. *Dalton Trans*. **2006**, *0*, 5327–5333.
[70] Winter, C. H. The Chemical Vapor Deposition of Metal Nitride Films Using Modern Metalorganic Precursors. *Aldrichimica Acta* **2000**, *33*, 3–8.
[71] Groom, C. R.; Bruno, I. J.; Lightfoot, M. P.; Ward, S. C. The Cambridge Structural Database. *Acta Cryst.* **2016**, *B72*, 171–179. DOI: 10.1107/S2052520616003954.
[72] Wächtler, E.; Gericke, R.; Brendler, E.; Gerke, B.; Langer, T.; Pöttgen, R.; Zhechkov, L.; Heine, T.; Wagler, J. Group 10−Group 14 Metal Complexes $[E{-}TM]^{IV}$: The Role of the Group 14 Site as an L, X, and Z-type Ligand. *Dalton Trans.* **2016**, *45*, 14252.
[73] Brendler, E.; Wächtler, E.; Heine, T.; Zhechkov, L.; Langer, T.; Pöttgen, R.; Hill, A. F.; Wagler, J. Stannylene or Metallastanna(IV)ocane: A Matter of Formalism. *Angew. Chem. Int. Ed.* **2011**, *50*, 4696–4700.
[74] Warsink, S.; Derrah, E. J.; Boon, C. A.; Cabon, Y.; de Pater, J. J. M.; Lutz, M.; Klein Gebbink, R. J. M.; Deelman, B-J. Intramolecularly Stabilised Group 10 Metal Stannyl and Stannylene Complexes: Multi-pathway Synthesis and Observation of Platinum-to-Tin Alkyl Transfer. *Chem. Eur. J.* **2015**, *21*, 1765–1779.
[75] Takaya, J. Nakamura, S.; Iwasawa, N. Synthesis, Structure, and Catalytic Activity of Palladium Complexes Bearing a Tridentate PXP-Pincer Ligand of Heavier Group 14 Element (X = Ge, Sn). *Chem. Lett.* **2012**, *41*, 967–969.
[76] Batsanov, S. S. Van der Waals Radii of Elements. *Inorg. Mater.* **2001**, *37*, 871–885.
[77] Yang, L.; Powell, D. R.; Houser, R. P. Structural Variation in Copper(I) Complexes with Pyridylmethylamide Ligands: Structural Analysis with a New Four-Coordinate Geometry Index, τ_4. *Dalton Trans.* **2007**, *9*, 955–964.
[78] Vela, J.; Cirera, J.; Smith, J. M.; Lachicotte, R. J.; Flaschenriem, C. J.; Alvarez, S.; Holland, P. L. Quantitative Geometric Descriptions of the Belt Iron Atoms of the Iron-Molybdenum Cofactor of Nitrogenase and Synthetic Iron(II) Model Complexes. *Inorg*. *Chem.* **2007**, *46*, 60–71.
[79] Becke, A. D. A New Mixing of Hartree-Fock and Local Density-Functional Theories. *J. Chem. Phys.* **1993**, *98*, 1372–1377.
[80] Zhao, Y.; Truhlar, D. G. The M06 Suite of Density Functionals for Main Group Thermochemistry, Thermochemical Kinetics, Noncovalent Interactions, Excited States, and Transition Elements: Two New Functionals and Systematic Testing of Four M06-Class Functionals and 12 other Functionals. *Theor*. *Chem. Acc.* **2008**, *120*, 215–241.
[81] Wächtler, E.; Gericke, R.; Zhechkov, L.; Heine, T.; Langer, T.; Gerke, B.; Pöttgen, R.; Wagler, J. Pyridine-2-thiolate Bridged Tin-Palladium Complexes with $Sn(PdN_2Cl_2)$, $Sn(PdN_2S_2)$, $Sn(PdN_2C_2)$ and $Sn(Pd_2N_4)$ Skeletons. *Chem. Commun.* **2014**, *50*, 5382–5384.
[82] Wieberg, K. B. Application of the People-Santry-Segal CNDO Method to the Cyclopropylcarbinyl and Cyclobutyl Cation and to Bicyclobutane. *Tetrahedron*, **1968**, *24*, 1083–1096.
[83] Rees, G. J.; Orr, S. T.; Barrett, L. O.; Fisher, J. M.; Houghton, J.; Spikes, G. H.; Theobald, B. R. C.; Thompsett, D.; Smith, M. E.; Hanna, J. V. Characterisation of Platinum-Based Fuel Cell Catalyst Materials Using ^{195}Pt Wideline Solid State NMR. *Phys. Chem. Chem. Phys.* **2013**, *15*, 17195–17207.
[84] Green, M. L. H. A New Approach to the Formal Classification of Covalent Compounds of the Elements. *J. Organomet. Chem.* **1995**, *500*, 127–148.
[85] Shaw, S.; Tian, X.; Silva, T. F.; Bobbit, J. M.; Naab, F.; Rodrigues, C. L.; Smith, E. A.; Cademartiri, L. Selective Removal of Ligands from Colloidal Nanocrystal Assemblies with Non-Oxidizing He Plasmas. *Chem. Mater.*, **2018**, *30*, 5961–5967.
[86] Shaw, S.; Colaux, J. L.; Hay, J. L.; Peiris, F. C.; Cademartiri, L. Building Materials from Colloidal Nanocrystal Arrays: Evolution of Structure, Composition, and Mechanical Properties upon the Removal of Ligands by O_2 Plasma. *Adv. Mater*. **2016**, *28*, 8900–8905.
[87] *XRD Standard Patterns*; Inorganic Crystal Structure Database: Karlsruhe, Germany, 2019.
[88] Fountoulaki, S.; Daikopoulou, V.; Gkizis, P. L.; Tamiolakis, I.; Armatas, G. S.; Lykakis, I. N. Mechanistic Studies of the Reduction of Nitroarenes by $NaBH_4$ or Hydrosilanes Catalyzed by Supported Gold Nanoparticles. *ACS Catal.* **2014**, *4*, 3504–3511.
[89] Vix, A. B. E.; Müller-Buschbaum, P.; Stocker, W.; Stamm, M.; Rabe, J. P. Crossover between Dewetting and Stabilization of Ultrathin Liquid Crystalline Polymer Films. *Langmuir* **2000**, *16*, 10456–10462.

[90] Ikeda, T.; Tsutsumi, O. Optical Switching and Image Storage by Means of Azobenzene Liquid-Crystal Films. *Science* **1995**, *268*, 1873–1875.
[91] Huang, J. M.; Kuo, J. F.; Chen, C. Y. Studies on Mesomorphic Behaviors of Segmented Azoxy Polyester Containing Polyoxyethylene. *J. Appl. Polym. Sci.* **1995**, *55*, 1217–1229.
[92] Kumar, G. S.; Neckers, D. C. Photochemistry of Azobenzene-Containing Polymers. *Chem. Rev.* **1989**, *89*, 1915–1925.
[93] Hamon, F.; Djedaini-Pilard, F.; Barbot, F.; Len, C. Azobenzenes—Synthesis and Carbohydrate Applications. *Tetrahedron* **2009**, *65*, 10105–10123.
[94] Chang, C.-F.; Liu, S.-T. Catalytic Oxidation of Anilines into Azoxybenzenes on Mesoporous Silicas Containing Cobalt Oxide. *J. Mol. Catal. Chem.* **2009**, *299*, 121–126.
[95] Pahalagedara, M. N.; Pahalagedara, L. R.; He, J.; Miao, R.; Gottlieb, B.; Rathnayake, D.; Suib, S. L. Room Temperature Selective Reduction of Nitrobenzene to Azoxybenzene Over Magnetically Separable Urchin-like Ni/Graphene Nanocomposites. *J. Catal.* **2016**, *336*, 41–48.
[96] Ghosh, S.; Acharyya, S. S.; Sasaki, T.; Bal, R. Room Temperature Selective Oxidation of Aniline to Azoxybenzene Over a Silver Supported Tungsten Oxide Nanostructured Catalyst. *Green Chem.* **2015**, *17,* 1867–1876.
[97] Chen, Y.-F.; Chen, J.; Lin, L.-J.; Chuang, G. J. Synthesis of Azoxybenzenes by Reductive Dimerization of Nitrosobenzene. *J. Org. Chem.* **2017**, *82*, 11626–11630.
[98] Rezaeifard, A.; Jafarpour, M.; Naseri, M. A.; Shariati, R. A Rapid and Easy Method for the Synthesis of Azoxy Arenes Using Tetrabutylammonium Peroxymonosulfate. *Dyes Pigments* **2008**, *76*, 840–843.
[99] Wächtler, E.; Gericke, R.; Kutter, S.; Brendler, E.; Wagler, J. Molecular Structures of Pyridinethiolato Complexes of Sn(II), Sn(IV), Ge(IV), and Si(IV). *Main Group Met. Chem.* **2013**, *36*, 181–191.
[100] Frisch, M. J.; Trucks, G. W.; Schlegel, H. B.; Scuseria, G. E.; Robb, M. A.; Cheeseman, J. R.; Scalmani, G.; Barone, V.; Mennucci, B.; Petersson, G. A.; Nakatsuji, H.; Caricato, M.; Li, X.; Hratchian, H. P.; Izmaylov, A. F.; Bloino, J.; Zheng, G.; Sonnenberg, J. L.; Hada, M.; Ehara, M.; Toyata, K.; Fukuda, R.; Hasegawa, J.; Ishida, M.; Nakajima, T.; Honda, Y.; Kitao, O.; Nakai, H.; Vreven, T.; Montgomery, J. A., Jr.; Peralta, J. E.; Ogliaro, F.; Bearpark, M.; Heyd, J. J.; Brothers, E.; Kudin, K. N.; Staroverov, V. N.; Kobayashi, R.; Normand, J.; Raghavachari, K.; Rendell, A.; Burant, J. C.; Iyengar, S. S.; Tomasi, J.; Cossi, M.; Rega, N.; Millam, J. M.; Klene, M.; Knox, J. E.; Cross, J. B.; Bakken, V.; Adamo, C.; Jaramillo, J.; Gomperts, R.; Stratmann, R. E.; Yazyev, O.; Austin, A. J.; Cammi, R.; Pomelli, C.; Ochterski, J. W.; Martin, R. L.; Morokuma, K.; Zakrzewski, V. G.; Voth, G. A.; Salvador, P.; Dannenberg, J. J.; Dapprich, S.; Daniels, A. D.; Farkas, O.; Foresman, J. B.; Ortiz, J. V.; Cioslowski, J.; Fox, D. J. *Gaussian 09, Revision A.02*; Gaussian, Inc.: Wallingford, CT, 2009.
[101] Grimme, S. Semiempirical GGA-Type Density Functional Constructed with a Long-Range Dispersion Correction. *J. Comput. Chem.* **2006**, *27*, 1787–1799.
[102] Hay, P. J.; Wadt, W. R. *Ab Initio* Effective Core Potentials for Molecular Calculations. Potentials for K to Au Including the Outermost Core Orbitals. *J. Chem. Phys.* **1985**, *82*, 299–310.
[103] Wadt, W. R.; Hay, P. J. *Ab Initio* Effective Core Potentials for Molecular Calculations. Potentials for Main Group Elements Na to Bi. *J. Chem. Phys.* **1985**, *82*, 284–298.
[104] Hariharan, P. C.; Pople, J. A. The Influence of Polarization Functions on Molecular Orbital Hydrogenation Energies. *Theor. Chim. Acta* **1973**, *28*, 213–222.
[105] Hehre, W. J.; Ditchfield, R.; Pople, J. A. Self-Consistent Molecular Orbital Methods. XII. Further Extensions of Gaussian-Type Basis Sets for Use in Molecular Orbital Studies of Organic Molecules. *J. Chem. Phys.* **1972**, *56*, 2257–2261.
[106] Andrae, D.; Häußermann, U.; Dolg, M.; Stoll, H.; Preuß, H. Energy-adjusted *Ab Initio* Pseudopotentials for the Second and Third Row Transition Elements. *Theor. Chim. Acta* **1990**, *77*, 123–141.
[107] Bergner, A.; Dolg, M.; Küchle, W.; Stoll, H.; Preuß, H. *Ab Initio* Energy-adjusted Pseudopotentials for Elements of Groups 13-17. *Mol. Phys.* **1993**, *80*, 1431–1441.
[108] Metz, B.; Stoll, H.; Dolg, M. Small-core Multiconfiguration-Dirac-Hartree-Fock-adjusted Pseudopotentials for Post-d Main Group Elements: Application to PbH and PbO. *J. Chem. Phys.* **2000**, *113*, 2563–2569.
[109] Peterson, K. A. Systematically Convergent Basis Sets with Relativistic Pseudopotentials. I. Correlation Consistent Basis Sets for the Post-d Group 13-15 Elements. *J. Chem. Phys.* **2003**, *119*, 11099–11112.
[110] Peterson, K. A.; Figgen, D.; Dolg, M.; Stoll, H. Energy-consistent Relativistic Pseudopotentials and Correlation Consistent Basis Sets for the 4d Elements Y-Pd. *J. Chem. Phys.* **2007**, *126*, 124101.
[111] Schuchardt, K. L.; Didier, B. T.; Elsethagen, T.; Sun, L.; Gurumoorthi, V.; Chase, J.; Li, J.; Windus, T. L. Basis Set Exchange: A Community Database for Computational Sciences. *J. Chem. Inf. Model* **200**, *47*, 1045–1052.
[112] Harris, R. K.; Becker, E. D.; Cabral de Menezes, S. M.; Goodfellow, R.; Granger, P. Nuclear Spin Properties and Conventions for Chemical Shifts. *Pure Appl. Chem.* **2001**, *73*, 1795–1818.

TOC